Monthly Notices of the ROYAL ASTRONOMICAL SOCIETY
MNRAS **454,** 3432–3444 (2015) doi:10.1093/mnras/stv2229

On the Eddington limit for relativistic accretion discs

Pavel Abolmasov[1,2]★ and Anna Chashkina[1,2]

[1]*Tuorla Observatory, Department of Physics and Astronomy, University of Turku, Väisäläntie 20, FI-21500 Piikkiö, Finland*
[2]*Sternberg Astronomical Institute, Moscow State University, 119992 Moscow, Russia*

Accepted 2015 September 23. Received 2015 September 17; in original form 2015 June 24

ABSTRACT

Standard accretion disc model relies upon several assumptions, the most important of which is geometrical thinness. Whenever this condition is violated, new physical effects become important such as radial energy advection and mass loss from the disc. These effects are important, for instance, for large mass accretion rates when the disc approaches its local Eddington limit. In this work, we study the upper limits for standard accretion disc approximation and find the corrections to the standard model that should be considered in any model aiming on reproducing the transition to super-Eddington accretion regime. First, we find that for thin accretion disc, taking into account relativistic corrections allows to increase the local Eddington limit by about a factor of 2 due to stronger gravity in general relativity (GR). However, violation of the local Eddington limit also means large disc thickness. To consider consequently the disc thickness effects, one should make assumptions upon the two-dimensional rotation law of the disc. For rotation frequency constant on cylinders $r\sin\theta = \mathrm{const}$, vertical gravity becomes stronger with height on spheres of constant radius. On the other hand, effects of radial flux advection increase the flux density in the inner parts of the disc and lower the Eddington limit. In general, the effects connected to disc thickness tend to increase the local Eddington limit even more. The efficiency of accretion is however decreased by advection effects by about a factor of several.

Key words: accretion, accretion discs – radiation: dynamics – relativistic processes – X-rays: general.

1 INTRODUCTION

Standard disc accretion introduced by Shakura & Sunyaev (1973) successfully explains the thermal component of the spectra of X-ray binaries (Done, Gierliński & Kubota 2007). It is also applied to explain the 'blue bumps' of the spectral of active galactic nuclei (AGNs) but here the success of the model is less certain (see for instance Lawrence 2012). Standard disc model relies on several assumptions, the most important of them connected to the 'thinness' of the disc meaning that the motion of the accreted matter does not differ significantly from Keplerian rotation in a plane passing through the accretor. Equations of vertical and radial structure may be decoupled then due to large differences in spatial scales and gradients in these two distinct directions. Thinness also implies 'locality' condition meaning that all the energy dissipated at some radius is radiated away at the same radius (because vertical radiation transfer is much faster).

The basic assumptions of the thin disc model are violated at low and high mass accretion rates. First is connected with the cooling time-scales that become very large for low densities (Meyer, Liu & Meyer-Hofmeister 2000b). At large mass accretion rates, on one hand, the cooling time-scales again become high because of the very high optical depths, while on the other hand, the radiation flux generated inside the disc becomes strong enough for the accretion disc to approach its Eddington limit.

When Eddington (1925) introduced the luminosity limit, he adopted spherical symmetry. But the geometry of a real astrophysical system may be different. The physics underlying the Eddington luminosity is force balance between gravity and radiation pressure determined primarily by the radiation flux.[1] Above a certain photosphere belonging to a star or an accretion disc, the limiting value for radiation flux is

$$F_{\mathrm{Edd}} = \frac{c}{\varkappa} g, \tag{1}$$

where $\varkappa$ is opacity (usually set to Thomson electron scattering opacity that equals $\varkappa \simeq 0.34\,\mathrm{cm^2\,g^{-1}}$ for Solar metallicity), c is the speed of light and g is the gravity in the direction normal to the photosphere. Spherical symmetry in classical mechanics implies

★ E-mail: pavel.abolmasov@gmail.com

[1] There are uncertainties connected to limb darkening and radiation collimation that we do not consider in this paper.

$F = L/4\pi R^2$ and $g = GM/R^2$ and hence there is a luminosity limit independent of distance:

$$L_{\rm Edd} = \frac{4\pi GMc}{\varkappa} \simeq 1.4 \times 10^{38} \frac{M}{{\rm M}_\odot} {\rm erg\,s^{-1}}. \quad (2)$$

If the luminosity is released by accretion processes, the upper limit for luminosity implies an upper limit for the mass accretion rate (as radiation pressure opposes matter infall) and hence

$$\dot{M}_{\rm max} \simeq \frac{1}{\eta}\frac{L_{\rm Edd}}{c^2}, \quad (3)$$

where η is accretion efficiency (radiation energy released per unit accreting mass). Again, such a limit assumes spherical symmetry.

On the other hand, in accretion discs, gravity (compensated by centrifugal force in radial direction) and radiation, both directed roughly vertically, depend on both the vertical and radial coordinates in the disc hence the radiation pressure limit should be applied locally. Vertical gravity becomes stronger with height, hence increase in local energy release may be compensated by increased disc thickness (we will hereafter use half-thickness H) up to a certain thickness comparable to the local radial coordinate ($H \sim R$) where the thin-disc approximation breaks down. Above this accretion rate value that we will call 'critical', accretion disc structure is significantly distorted inside the outermost radius where the disc becomes thick (spherization radius, see Shakura & Sunyaev 1973, section IV). Radiation pressure becomes most important in the inner parts of the disc where one should take into account general relativity (GR) effects to estimate rigorously the real limit when standard disc accretion approximation is violated. In this paper, we attempt to estimate accurately where does a radiatively efficient relativistic disc become supercritical and find that the Eddington limit is scaled up by a factor of several due to geometrical and GR effects.

The article is organized as follows. In Section 2, we consider the spherization radius and estimate the critical mass accretion rate in the thin-disc approximation taking into account relativistic corrections. In Section 3, we consider the different effects connected to disc thickness that appear to make the effective Eddington limit even higher and besides change some of the properties of near-standard discs below the Eddington limit. In Section 4, we discuss the limitations of our approach and make conclusions.

2 THIN DISC APPROXIMATION

Thin accretion disc as introduced by Shakura & Sunyaev (1973) was historically the first accretion disc model successfully applied to explain the observational properties of the discs in X-ray binaries and AGNs. Fully relativistic thin accretion disc model was introduced by Novikov & Thorne (1973). Vertical radiation flux in comoving frame

$$F = \frac{3}{8\pi}\frac{GM\dot{M}}{R^3}\frac{\mathcal{Q}}{\mathcal{B}\sqrt{\mathcal{C}}} = \frac{3}{2}\frac{c^5}{\varkappa GM}\frac{\dot{m}}{r^3}\frac{\mathcal{Q}}{\mathcal{B}\sqrt{\mathcal{C}}}, \quad (4)$$

where $r = \frac{Rc^2}{GM}$ is normalized radius, $\dot{m} = \frac{\dot{M}c^2}{L_{\rm Edd}} = \frac{\dot{M}\varkappa c}{4\pi GM}$ is normalized mass accretion rate, and calligraphic letters correspond to the coefficients introduced and calculated by Novikov & Thorne (1973) and Page & Thorne (1974):

$$\mathcal{B} = 1 + \frac{a}{r^{3/2}}, \quad (5)$$

$$\mathcal{C} = 1 - \frac{3}{r} + \frac{2a}{r^{3/2}}, \quad (6)$$

$$\mathcal{Q} = \frac{\mathcal{B}}{\sqrt{r\mathcal{C}}}\left(\sqrt{r} - \sqrt{r_{\rm in}} - \frac{3}{4}a\ln\frac{r}{r_{\rm in}} - A_1 - A_2 - A_3\right), \quad (7)$$

where

$$A_1 = \frac{3(x_1-a)^2}{x_1(x_1-x_2)(x_1-x_3)}\ln\left(\frac{\sqrt{r}-x_1}{\sqrt{r_{\rm in}}-x_1}\right), \quad (8)$$

$x_{1,2,3}$ are solutions of the equation $x^3 - 3x + 2a = 0$, and A_2 and A_3 are obtained from A_1 using cyclic permutation $1 \to 2 \to 3$.

Radiation pressure is opposed by the vertical gravity that was first calculated by Riffert & Herold (1995) in the $z/R \ll 1$ limit. Comoving vertical gravity is given as

$$g_z = \frac{GMz}{R^3}\frac{C_{\rm r}}{\mathcal{C}}, \quad (9)$$

where

$$C_{\rm r} = 1 - \frac{4a}{r^{3/2}} + \frac{3a^2}{r^2}. \quad (10)$$

For a thin disc, vertical gravity is always proportional to the vertical coordinate z. At some height radiation pressure becomes balanced by the vertical gravity:

$$z = \frac{3}{2}\dot{m}\frac{GM}{c^2}\frac{\mathcal{Q}}{\mathcal{B}}\frac{\sqrt{\mathcal{C}}}{C_{\rm r}}. \quad (11)$$

This quantity has the physical meaning of the height of a radiation-pressure-supported accretion disc. It is also useful as an estimate for the so-called spherization radius at which the thin disc approximation breaks down. Since the vertical gravity approaches maximum at $z \sim R$, this puts also the local Eddington limit for the mass accretion rate. A fully relativistic expression for the spherization radius may be given in implicit form:

$$r_{\rm sph} = \frac{3}{2}\dot{m}\cdot\frac{\mathcal{Q}(r_{\rm sph},a)}{\mathcal{B}(r_{\rm sph},a)}\frac{\sqrt{\mathcal{C}}(r_{\rm sph},a)}{C_r(r_{\rm sph},a)}. \quad (12)$$

This expression may be solved numerically for $r_{\rm sph}$. The load of coefficients on the right-hand side approaches unity at large radii, but the approach is slow enough to produce strong deviations from the classical value of $r_{\rm sph} = \frac{3}{2}\dot{m}$ given by Shakura & Sunyaev (1973). These coefficients incorporate both relativistic effects and the inner boundary condition at $r = r_{\rm in}$ (at the last stable orbit radius). It is instructive to compare expression (12) with its non-relativistic analogue taking into account only the inner boundary condition (Abolmasov & Shakura 2012a):

$$r_{\rm sph,NR} = \frac{3}{2}\dot{m}\frac{4}{3}\cos^2\left(\frac{1}{3}{\rm acos}\left(-\frac{3\sqrt{r_{\rm in}}}{\sqrt{2\dot{m}}}\right)\right). \quad (13)$$

In this approximation, spherization radius exists only if $\dot{m} > \dot{m}_{\rm cr} = 4.5r_{\rm in}$. In Fig. 1, we compare these two estimates. For accretion rates $\dot{m} \lesssim 1000$, relativistic corrections alter the spherization radius by about 20 per cent. In Fig. 1, solid curves correspond to the GR case, and dashed to non-relativistic approximation. In both cases, middle curves correspond to the Schwarzschild case ($a = 0$) and the right and the left curves – to a moderate Kerr case with $a = 0.9$ assuming co- and counter rotation, correspondingly.

Equation (12) has no solutions if mass accretion rate is small enough. If mass accretion rate is large enough, there are two solutions, the larger of which is interpreted as the spherization radius. The minimal $\dot{m}$ value where the equation has a solution has the physical meaning of critical mass accretion rate. While the spherization radius changes slightly due to relativistic effects, the critical mass accretion rate defined this way increases by about a factor of 3. In Fig. 2, we compare the critical mass accretion rates defined straightforward as $L_{\rm Edd}/\eta(a)c^2$, and non-relativistic and relativistic

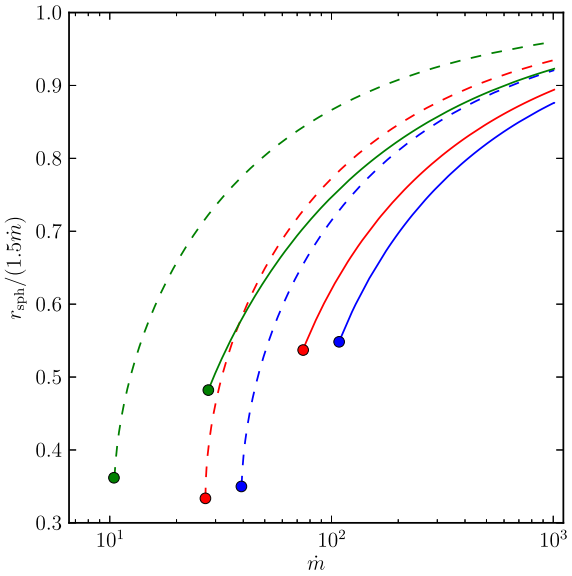

Figure 1. Spherization radii calculated according to relativistic (solid lines) and non-relativistic (dotted) formulae. Thick dots mark the critical accretion rate for the relevant Kerr parameter value. The curves and dots were calculated for three different Kerr parameter values: $a = 0$ (red, middle curves), $a = 0.9$ (assuming corotation; blue, rightmost curves) and $a = -0.9$ (counter rotation; green, leftmost curves).

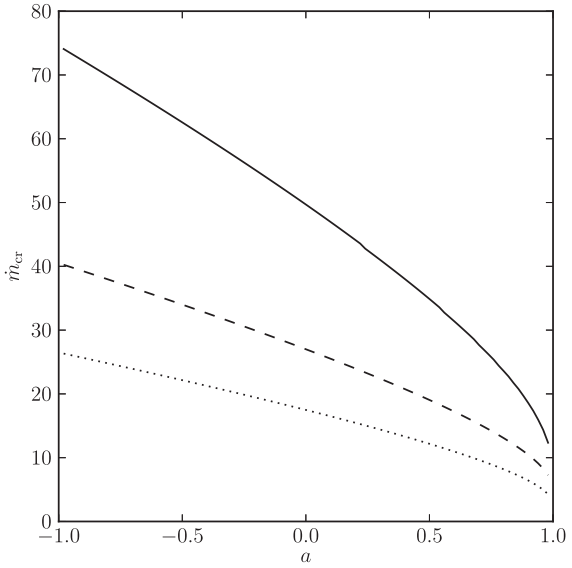

Figure 2. Critical mass accretion rate as a function of Kerr parameter a (negative a corresponds to counter rotation). Dotted line is the critical accretion rate for spherically symmetric accretion $[\eta^{-1}(r_{\rm in}, a)]$, dashed line is the maximal mass accretion rate in Newtonian approximation, and the solid line corresponds to the limit in full GR.

critical mass accretion rates defined through local radiation pressure balance condition. Here, the dotted line shows the limiting mass accretion rate in the spherically symmetric case, equal to $\eta^{-1}(r_{\rm in}, a)$. The dashed curve corresponds to a thin Newtonian disc while the solid curve takes into account GR effects.

3 CORRECTIONS FOR DISC THICKNESS

3.1 The issue of disc thickness

As real accretion discs become thick near the Eddington limit, it is instructive to check whether neglecting accretion disc thickness introduces any important corrections into the vertical balance. Disc 'thickness' is in fact a complex of several physical effects connected to violation of the basic assumptions of the thin-disc approximation, including the following.

(i) geometrical thickness and, as a consequence, non-linear dependence of the vertical gravity on height,
(ii) non-Keplerian rotation and differential rotation with vertical coordinate that may lead to additional angular momentum transfer in vertical direction; this also affects dissipation and energy release inside the disc,
(iii) violation of local energy release approximation due to both advection and radial flux diffusion,
(iv) existence of radial and meridional velocity fields.

Here, we will try to approximately account for the first, the third and the partly the second correction. We will assume constant rotation frequency on cylindrical surfaces $\varpi = r\sin\theta = \text{const}$, where θ is polar angle. This is close to the rotation law expected in barotropic case where rotation frequency should be constant on the so-called von Zeipel cylinders (Abramowicz 1971). In Appendix A, we show that the shapes of von Zeipel cylinders are indeed very close to cylinders in Boyer–Lindquist coordinates practically everywhere except inside the ergosphere. Accretion disc enters the ergosphere only for very large rotation parameters $a \gtrsim 0.94$. Outside the ergospheric region, for a fixed cylindrical coordinate $\varpi = r\sin\theta$, rotation frequency always grows with height that implies faster rotation (and, consequently, stronger effective gravity) at a surface for constant spherical coordinate r. Hence using coordinate cylinders $\varpi = \text{const}$ we underestimate the growth of the gravity with height.

3.2 Numerical simulations

Numerical simulations of thick magnetohydrodynamic (MHD) discs support the assumption of Keplerian rotation in the inner parts of thick accretion discs and even inside the last stable orbit (Penna et al. 2010). We have considered the results of a thick-disc MHD simulation from Abolmasov (2014), namely the run B1h presented in this work. Simulation was performed using the numerical code HARM2D that solves ideal MHD equations in Kerr metric (Gammie, McKinney & Tóth 2003; Noble et al. 2006). The main goal of the simulation was to form a moderately thin disc ($H/R \sim 0.1$) around a Kerr ($a = 0.9$) black hole and consider the motion of the matter inside the inner edge of the disc. As the initial conditions, an exact relativistic torus solution by Fishbone & Moncrief (1976), section IIIb, was used with small magnetic fields introduced that are subsequently amplified by MHD instabilities in the disc. Amplified magnetic fields lead to outwards angular momentum transfer and consequently to accretion from the torus through a moderately thick disc formed during the first 2000 dynamical time-scales (GM/c^3) of the simulation. We also use the simulation run A50s presented in Abolmasov (2014) that was calculated for $a = 0$ and multiloop initial magnetic field and uses smaller resolution. Main details of the simulations used in the present paper are given in Table 1.

A thicker torus in the model of Fishbone & Moncrief (1976) is also more extended in radial direction. As the result, it may become impossible to maintain the boundary condition at the outer

Table 1. HARM model parameters, including the parameters of the initial Fishbone–Moncrief torus, $r_{\rm max}$ (radius of maximal specific enthalpy) and $r_{\rm in}$ (inner radius) are also given. The time ranges (in GM/c^3) used for averaging are also given.

Model	Resolution	a	$r_{\rm max}$	$r_{\rm in}$	Number of loops	Time range
B1h	192×320	0.9	8.4	4.8	1	2000–5700
A50s	128×192	0	19.7	12.8	50	10 000–15 000
D1	128×192	0.99	10	4	1	2000–5700

boundary, and the simulation becomes unstable. A way around is to consider a black hole with a higher Kerr parameter. More rapid rotation allows to produce a thicker disc without making the initial torus model extended beyond the simulation domain. Apart from the models described in Abolmasov (2014), we have calculated a similar model with a higher Kerr parameter, $a = 0.99$. Absence of heating and cooling sources in HARM2D makes it difficult to simulate very thick as well as very thin discs. While the initial torus has $H/R \sim 0.5$, the accretion disc forms from its inner cusp that has lower geometrical thickness. For the B1h model, the relative thickness is $H/R \simeq 0.1$ as measured by Gaussian fitting, while for the model with $a = 0.99$ that we will hereafter dub as D1, the thickness was around 0.2. In fact, all the equilibrium torus models, however thick, have smaller thicknesses near the inner rim (see, for example, Penna, Kulkarni & Narayan 2013, Fig. 3).

Surprisingly, in all our models, not only the lines of constant angular velocity are close to cylinders $\varpi = r\sin\theta = {\rm const}$ but the rotation law between $r \simeq 2$ and $r \simeq 10$ conforms with Keplerian rotation with about 3–4 per cent accuracy (relative standard deviation from the Keplerian law) for $\theta \gtrsim 45^\circ$. For larger distances from the equatorial plane, rotation becomes strongly sub-Keplerian. On the other hand, in the equatorial plane, Keplerian rotation holds to about 1 per cent. In Figs 3 and 4 (left-hand panels), lines of constant angular frequency ($\Omega = u^\varphi/u^t$) are shown and compared to the Keplerian rotation law ($\Omega_{\rm K} = (\varpi^{3/2} + a)$), and the lines of constant angular frequency are shown to conform well with the cylinders $\varpi = {\rm const}$. Keplerian rotation holds even inside the last stable orbit.

Our results are at odds with some of the comprehensive thick-disc simulations such as by Sądowski et al. (2014) that, for a similar set-up, find rotation sub-Keplerian by not less than 15 per cent, both outside and inside the last stable orbit (see Fig. 11 in this work). On the other hand, Shafee et al. (2008), for instance, find the angular momentum close to Keplerian just outside the last stable orbit. The overall behaviour of the net angular momentum in the simulations by Shafee et al. (2008) conforms well with the conventional picture of hydrodynamic transonic accretion: nearly Keplerian rotation outside the last stable orbit, Keplerian rotation at the sonic surface and roughly constant angular momentum (u_φ) in the supersonic region. On the other hand, Sądowski et al. (2014) find the net angular momentum rapidly decreasing inside the last stable orbit.

The reason for this discrepancy lies probably in the diverse structure of magnetic field formed during disc accretion with frozen-in magnetic fields (Penna et al. 2010). The initial conditions include small seed magnetic field subsequently amplified by MHD instabilities. Amplified poloidal magnetic fields are then advected towards the black hole and contribute to the accumulated magnetic flux through the black hole horizon. This magnetic flux grows gradually with time that leads to secular evolution of the deviations from Keplerian rotation. In simulations B1h and D1, we assumed the initial magnetic field potential scaling with the rest-mass density as $A_\varphi \propto \rho$. However, in Sądowski et al. (2014), the magnetic field obeys a different, more complicated law making it stronger further from the black hole. This leads to a gradual increase in magnetization of the accreting matter even during quasi-stationary accretion (see also Fig. 6 of Sądowski et al. 2014).

We conclude that the rotational structure of the inner disc and especially the flow inside the last stable orbit is strongly affected by the magnetic fields and especially by the magnetic field flux accumulated inside the disc. Our results should work as long as the large-scale magnetic field is dynamically unimportant. For the time span of the B1h simulation, rotation law changes very weakly after the establishment of quasi-stationary accretion at $t \sim 2000\,GM/c^3$, but simulations containing more complicated magnetic fields like A50s show irregular variations due to changes in magnetic field strength and geometry (see Fig. 5). Angular momenta given in this figure are density-weighed vertically averaged values (as in Sądowski et al. 2014).

In our simulations, rotation frequency is everywhere in the thick disc close to the following 'cylindrical Keplerian' law:

$$\Omega(r,\theta) = \frac{1}{\varpi^{3/2} + a}. \tag{14}$$

Estimating the two-dimensional rotational velocity field is crucial for the vertical structure of the disc since the vertical structure of the disc is determined by the deviations from the balance between inertial and gravitational forces, the former dependent upon the rotation law. There is no clear distinction between gravity and inertia in GR, and the vertical hydrostatic balance in accretion disc may be alternatively viewed as a balance between pressure gradients in the disc and the centrifugal force (Abramowicz, Lanza & Percival 1997).

3.3 Corrections for vertical gravity

Let us use spherical coordinates and consider the balance of radiation pressure and inertial forces (including gravity) along the polar angle θ. It is more convenient to use $\mu = \cos\theta$ instead of the angle itself or the vertical distance z. Relevant metric coefficient is

$$g_{\mu\mu} = g_{\theta\theta}\left(\frac{{\rm d}\theta}{{\rm d}\mu}\right)^2 = \rho^2/(1-\mu^2). \tag{15}$$

Then, considering a sphere of $r = {\rm const}$, one can express the 'vertical' free-fall acceleration as

$$g_\mu = -\Omega_\mu^2 \mu = \Gamma_{i\mu k} u^i u^k, \tag{16}$$

where i and k may be equal to t or φ, $u^\varphi = \Omega u^t$, and u^t is recovered from normalization condition $u_i u^i = -1$ (we neglect the radial and meridional velocities here). Vertical gravity should be compared to the coordinate flux component $F_\mu = F\sqrt{g_{\mu\mu}}$ multiplied by $\varkappa/c$ (see Section 3.4). All the relevant non-zero Christoffel symbols are $\Gamma_{i\mu k} = \frac{1}{2} g_{ik,\mu}$:

$$\Gamma_{t\mu t} = -\frac{2a^2 r}{\rho^4}\mu, \tag{17}$$

$$\Gamma_{t\mu\varphi} = \Gamma_{\varphi\mu t} = \frac{2ar\left(r^2+a^2\right)}{\rho^4}\mu, \tag{18}$$

$$\Gamma_{\varphi\mu\varphi} = -\tfrac{1}{\rho^4}\left(a^2(1-\mu^2)\Sigma^2 + \rho^2\Sigma^2 - a^2\Delta(1-\mu^2)\right)\mu = \\ = -\frac{r^6 + a^2r^4 + 4a^2r^3 + 2a^4 r + a^2\Delta\rho^2\mu^2}{\rho^4}\mu. \tag{19}$$

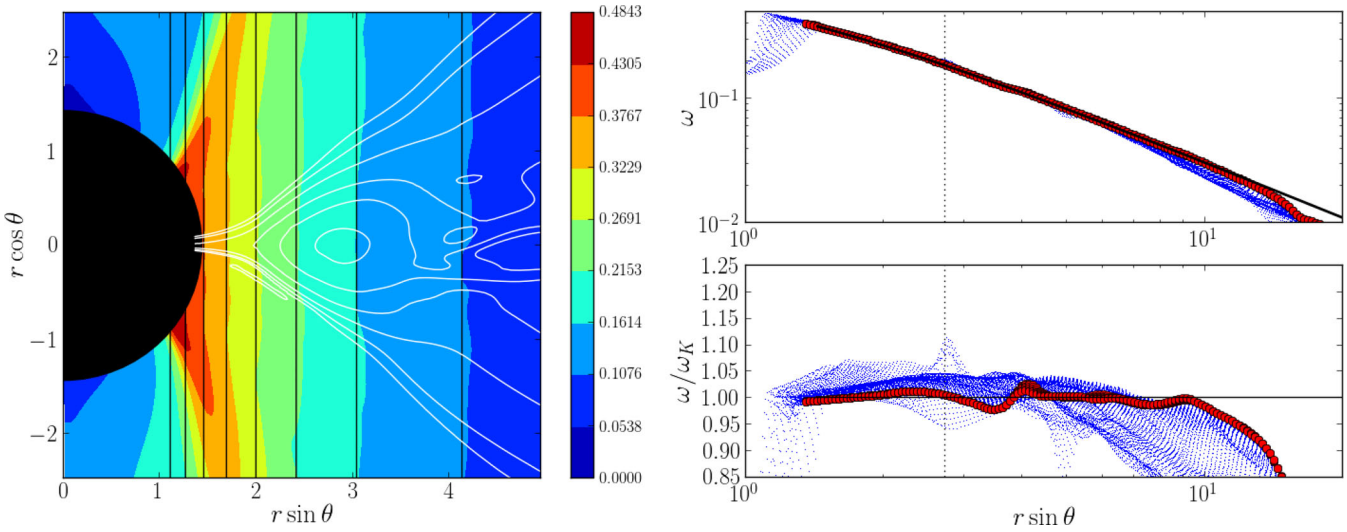

Figure 3. HARM2D simulation snapshot ($t = 5600\,GM/c^3$, B1h simulation from Abolmasov 2014). Left-hand panel: colour-coded is angular velocity $\Omega = u^{\varphi}/u^{t}$ in c^3/GM units, black lines are vertical ($\varpi = \text{const}$) lines corresponding to the same values of angular velocity as the boundaries between different colours/shades. Right-hand panels: angular frequency slice through the equatorial plane (thick red points) and for all the points with polar angle cosines $|\mu| < 1/\sqrt{2}$; solid black line is Keplerian law $\omega = ((r\sin\theta)^{3/2} + a)^{-1}$. Lower right panel shows relative deviations from the cylindrical Keplerian law. All the distances are in GM/c^2 units. Vertical dotted lines mark the radius of the last stable orbit.

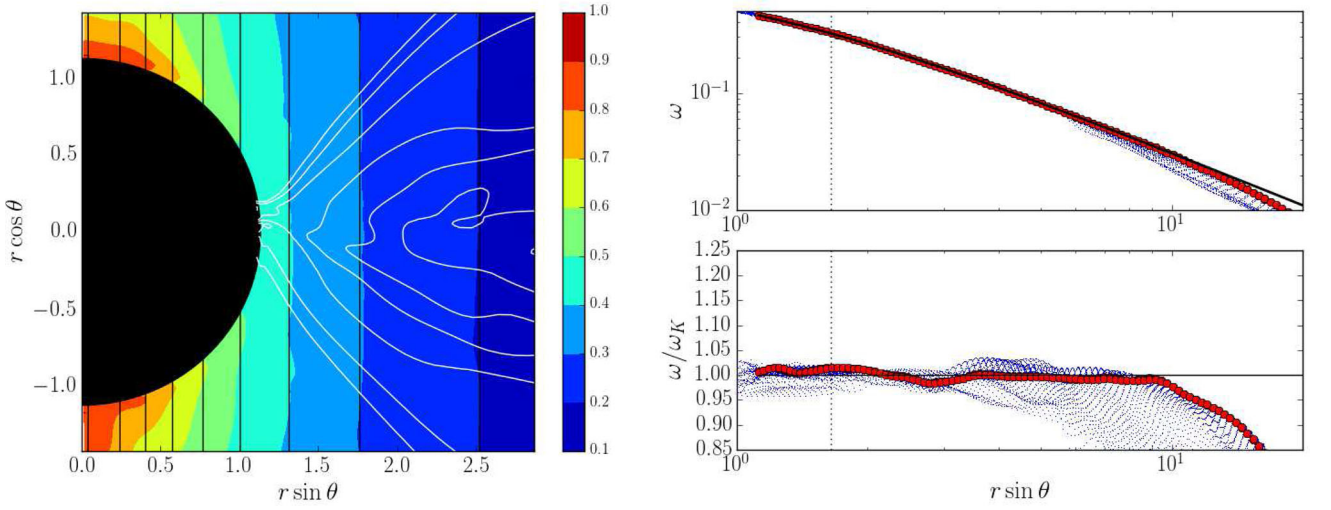

Figure 4. HARM2D simulation snapshot ($t = 5400\,GM/c^3$, D1 simulation with $a = 0.99$). Notation is the same as in the previous figure.

Substituting these expressions in the expression for g_{μ}, up to second order in μ

$$\Omega_{\mu}^2 = -\frac{1}{r}\left(\frac{C_r}{\mathcal{C}} + \frac{3}{2}\frac{\zeta(r,a)}{\mathcal{C}^2\mathcal{B}}\mu^2\right), \tag{20}$$

where

$$\zeta(r,a) = 1 - \frac{8}{3}\frac{1}{r} + \frac{a^2}{r^2} + \frac{14}{3}\frac{a^2}{r^{5/2}} - \frac{23}{3}\frac{a^2}{r^3} + \frac{16}{3}\frac{a^3}{r^{7/2}} + \\ + \frac{2}{3}\frac{a^2(7-4a^2)}{r^4} - 12\frac{a^3}{r^{9/2}} + 17\frac{a^4}{r^5} - \\ - \frac{8}{3}\frac{a^3(1+3a^2)}{r^{11/2}} - \frac{16}{3}\frac{a^4}{r^6} + \frac{38}{3}\frac{a^5}{r^{13/2}} - \frac{16}{3}\frac{a^6}{r^7}. \tag{21}$$

In such an approach, for most radii and Kerr parameter values, the effective vertical frequency becomes higher away from the equatorial plane if the spherical radial coordinate is held fixed. This effect arises from the assumption $\Omega = \Omega(r\sin\theta)$ that leads to effectively super-Keplerian rotation near the disc surface. If one considers a more realistic rotation law with Ω constant on von Zeipel cylinders, the effect becomes even stronger, except the most rapidly rotating black holes ($a \gtrsim 0.95$) where the inner parts of the disc exist inside the ergosphere, where the shapes of von Zeipel cylinders change considerably (see Appendix A). In our assumptions, ζ and thus the whole next-order correction is always positive. We also assume that the maximal possible thickness of the disc is $\mu_{\max} = 1/\sqrt{2}$.

3.4 Advection

Local energy flux in an axisymmetric disc consists of diffusion and advection terms, the latter directed along the local poloidal velocity. If the advection term is small compared to vertical diffusion, its overall effect is to shift downstream the thermal energy generated in the disc. Weak advection in a moderately thick disc may be approximately taken into account by introducing a 'delayed radius'

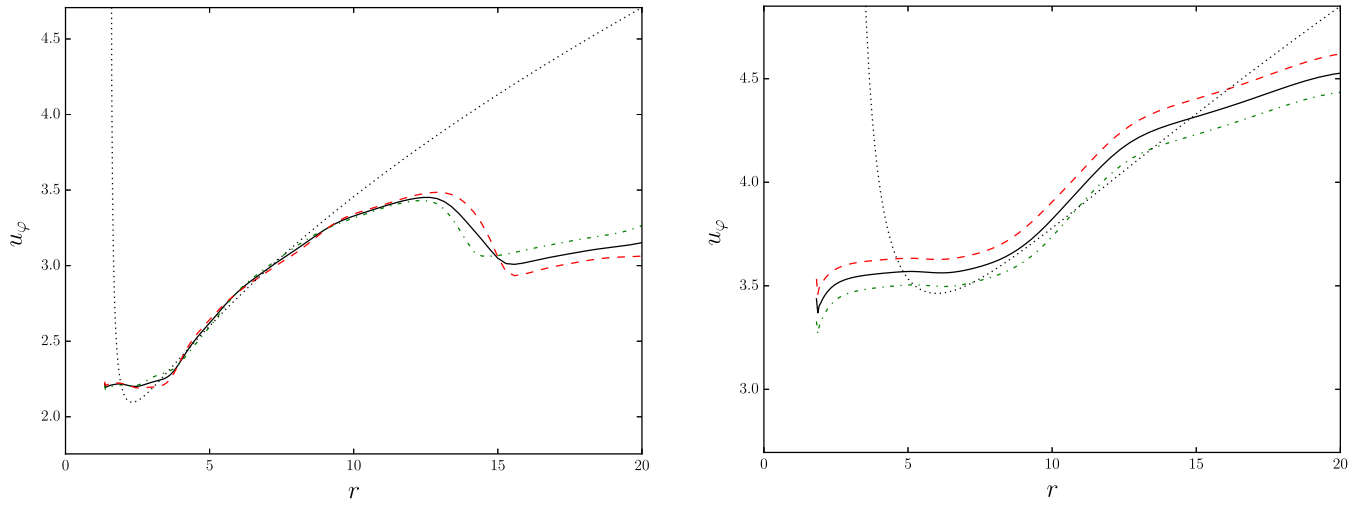

Figure 5. Radial profiles of density-weighed specific angular momenta for two simulations B1h (left) and A50s (right). Black solid curves are averages for all the frames of the quasi-stationary phase, green dot–dashed and red dashed curves show the averages calculated for the first and second halves of the period of time that we interpret as quasi-stationary accretion (2000–5700 GM/c^3 for B1h, 10 000–15 000 GM/c^3 for A50s). Keplerian net angular momentum is shown by dotted lines.

assumption that the flux generated at radial distance r_0 will be then emitted at a smaller radius $r = r_0 - \delta r(r_0)$. For our purposes, this approach is better than assuming a fixed fraction of liberated energy stored in the thermal energy of the disc as is it often done when considering discs with advection (Narayan & Yi 1995; Sądowski 2011), since it does not include unknown free parameters and can account for advection dependence on radius. Apart from the pure flux advection, one should take into account that the frame where the flux is compared to the vertical gravity is different from the frame (or frames) where the energy is generated that we would further identify with the comoving equatorial frame in the disc. Radial shift δr is a result of interplay between vertical energy diffusion and radial drift:

$$\delta r \simeq v_{\rm r} t_{\rm diff}, \tag{22}$$

where v_r is the radial velocity measured in the reference frame comoving with the disc, $t_{\rm diff} = H\tau_{\rm v}$, where $H = r\mu_{\rm max}$, and $\tau_{\rm v} = \frac{1}{2}\varkappa\Sigma$ is the vertical optical depth between the equatorial plane and the disc surface:

$$\delta r \simeq \frac{\mu_{\rm max}\dot{m}}{2}. \tag{23}$$

The main simplification is that the flux generated at the radial coordinate r_0 is emitted in a narrow radius interval near r. A reasonable assumption is also to assume all the flux generated near the equatorial plane and then conserved. More precisely, let us consider the energy flux due to radiation $T^k_t = u_t F^k + u^k F_t$ and integrate it upon a $\mu = \mu_{\rm max}$ surface just above the surface of the disc. Conservation of the energy flux implies:

$$T^k_t \sqrt{-g}{\rm d}S_k = {\rm const}, \tag{24}$$

for a given flux tube with cross-section given by the four-vector ${\rm d}S_k$. Setting the cross-section tangent to the $\theta = {\rm const}$ surface implies

$$u_t F^\mu \sqrt{-g}{\rm d}S_\mu = {\rm const}, \tag{25}$$

or

$$u^{\rm (s)}_t \sqrt{-g_{\rm (s)}}\frac{F_{\rm (s)}}{\sqrt{g^{\rm (s)}_{\mu\mu}}}{\rm d}r_{\rm (s)}{\rm d}\varphi = u^{\rm (d)}_t \sqrt{-g_{\rm (d)}}\frac{F_{\rm (d)}}{\sqrt{g^{\rm (d)}_{\mu\mu}}}{\rm d}r_{\rm (d)}{\rm d}\varphi, \tag{26}$$

where quantities with '(d)' index refer to the equatorial plane, and with '(s)' index – to the disc surface, $g = -\rho^4$ is metric determinant (hence $g_{\rm (d)} = -r_0^4$). Since ${\rm d}r_{\rm (d)} = {\rm d}r_{\rm (s)}$ (see above expression 23 for δr), area distortion is connected only to the difference in $\sqrt{-g}$ factors, incorporating relativistic effects and spherical geometry. Comoving flux at the surface of the thick disc is given as

$$F_{\rm (s)} = \frac{r_{\rm (d)}}{\rho_{\rm (s)}\sin\theta}\frac{u^{\rm (d)}_t}{u^{\rm (s)}_t}F_{\rm (d)}. \tag{27}$$

All the quantities with a '(d)' index on the right-hand side should be evaluated at r_0, and θ is the half-opening angle of the disc. Eddington limit in polar angle direction is written as

$$\frac{\varkappa}{c}F_{\rm (s)}\sqrt{g_{\mu\mu}} = \Omega^2_\mu \mu, \tag{28}$$

where Ω_μ is given by expression (20), and flux $F_{\rm (s)}$ by expression (27).

3.5 Effects of disc thickness upon the local Eddington limit

The effects of non-locality (including advection) are ambiguous: flux increases due to geometrical effects, and decreases due to decreasing dependence $F(r)$ everywhere except the innermost parts where the disc releases more energy than a standard disc. In Fig. 6, flux dependence on radius is shown taking into account advection and the geometrical effects described in Section 3.4. Note that for very high mass accretion rates ($\dot{m} \gtrsim 10^3$) advection is able to prevent the disc from surpassing the local Eddington limit. Our approximation does not reproduce this regime but it can definitely appear when advection becomes strong and essentially non-linear. This advection-dominated regime may be loosely identified with the slim-disc solution (Abramowicz et al. 1988; Sądowski 2011).

In Fig. 7, critical mass accretion rates calculated with and without corrections for disc thickness (including advection) are shown. As in Fig. 2, dotted line corresponds to the spherically symmetric case, and dashed line to the thin non-relativistic disc. Blue line (marked with a 'T' in the figure) shows the thin relativistic disc case considered in Section 2. However, the limiting disc thickness is taken to be $(H/R)_{\rm max} = 1/\sqrt{2}$ (since R is interpreted as spherical rather than

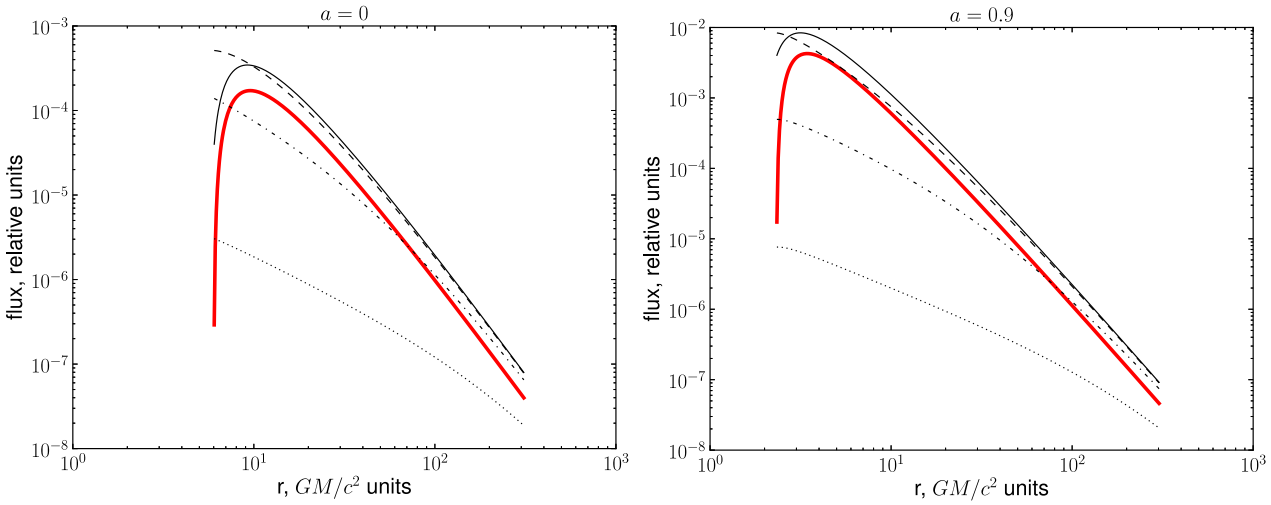

Figure 6. Flux dependence on radius for different mass accretion rates. Fluxes are divided by the mass accretion rate hence the highest fluxes correspond to the smallest $\dot{m}$ where advection is smaller. The thick red curve shows the standard accretion disc model, thin black curves correspond to $\dot{m} = 1$, 10, 100 and 1000 (solid, dashed, dash–dotted and dotted lines, respectively). Left- and right-hand panels show the cases of $a = 0$ and $a = 0.9$.

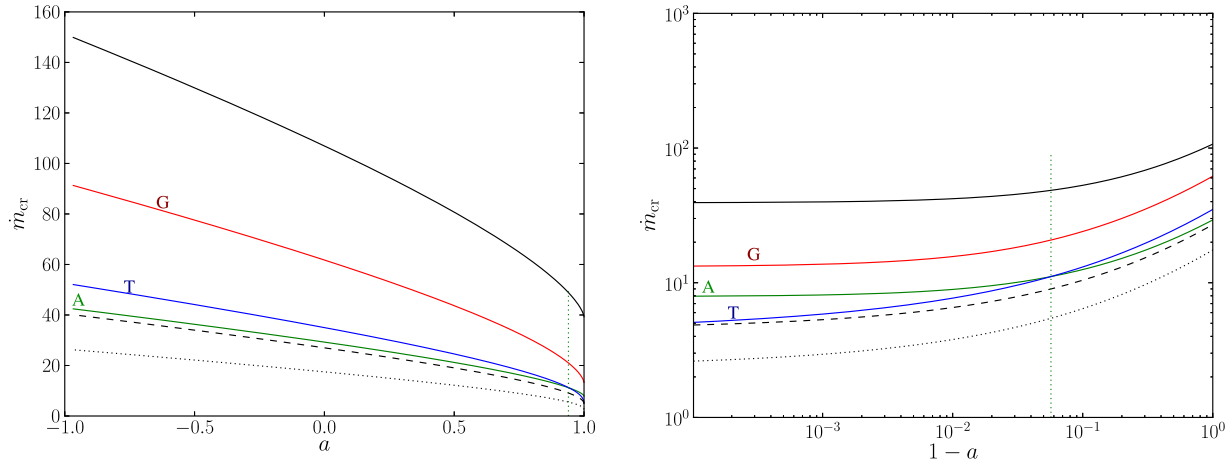

Figure 7. Critical mass accretion rate as a function of Kerr parameter. Left- and right-hand panels differ only in abscissa: in the left, it is linear in a, in the right, it is made logarithmic in $1 - a$ to resolve the behaviour of limiting mass accretion rates at high-mass accretion rates. Dotted and dashed black curves are identical to those in Fig. 2, corresponding to spherical and disc non-relativistic Eddington limit, correspondingly. The solid blue line (also marked as 'T') corresponds to the local thin relativistic disc Eddington limit. It goes somewhat lower than the solid line in Fig. 2 because the accretion disc thickness is limited by $\mu = 1/\sqrt{2}$ rather than $\mu = 1$. Green curve (marked by 'A') takes into account advection only, and red curve (marked by 'G') only second-order corrections to vertical gravity. Solid black curve accounts for both effects. Vertical dotted line marks the change of sign in ζ correction at the inner rim of the disc.

cylindrical coordinate; this is also close to the maximal polar angle cosine where cylindrical rotation holds in the HARM2D simulation we mention above) that decreases the critical rate. Red (subscribed with a 'G' in the figure) and green (marked 'A') curves show the effects of gravity and advection taken separately, and the solid black curve is calculated taking into account both effects. The critical mass accretion rates are shown as functions of Kerr parameter a. Same critical mass accretion rates are also shown as functions of $1 - a$ in logarithmical scale that allows to show in detail the limit of rapid black hole rotation.

Evidently, corrections to vertical gravity increase the value of the Eddington limit, at least for $a \lesssim 0.96$. However, the resulting values of the critical mass accretion rate are not much larger than the thin-disc estimate. While an account of advection and pure spherical geometry effects described in Section 3.4 in fact *decreases* the local Eddington limit because the local flux in the inner parts of the disc increases, stronger vertical gravity acts in the opposite direction. Including both effects simultaneously increases the local flux limit even more than gravity alone because at larger $\dot{m}$, advection effects decrease the local flux. The minimal possible spherization radius also becomes considerably larger because in the inner parts of the accretion disc, advection becomes too strong. Summarizing, we conclude that different effects connected to disc thickness produce corrections of different signs, but the general result holds and becomes even stronger.

3.6 Zone *a* disc thickness

Physical meaning of condition (28) is vertical balance between radiation and gravity, it can also be solved for μ to estimate the vertical scale of the disc. In Fig. 8, we compare the vertical scales of the discs for $\dot{m} = 30$ and different Kerr parameters. We find that disc thickness corrections decrease the vertical scale in the hottest and thickest parts of the disc while its inner rim attains finite

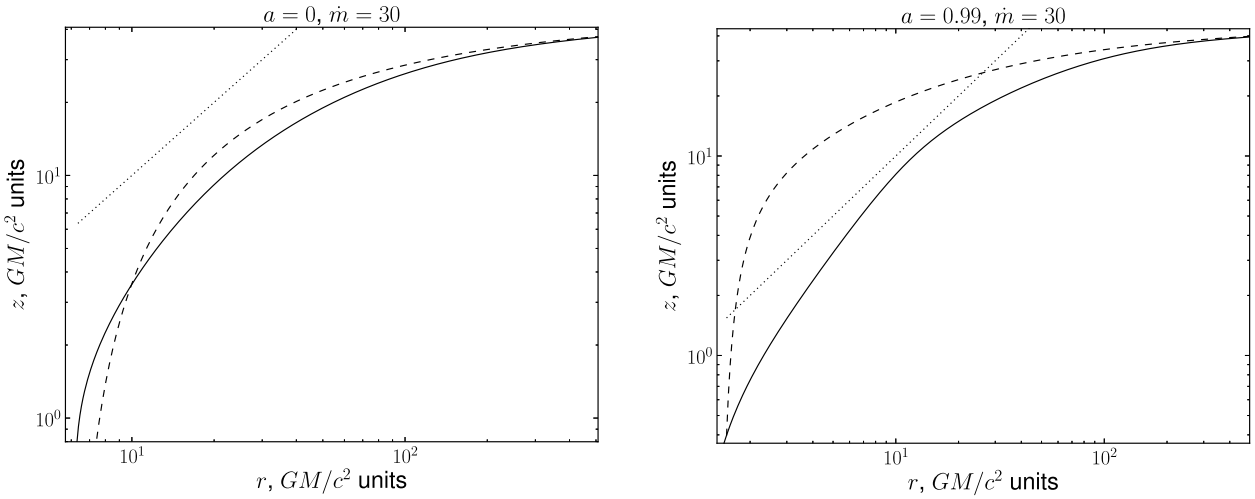

Figure 8. Disc vertical scales calculated taking into account corrections for vertical gravity and advection (solid lines). Dashed lines are standard disc zone a thicknesses for identical parameters. Dotted straight lines correspond to $z = r$.

thickness. At high mass accretion rates, the thickest part of the disc shifts to larger distances, and the surface inside the thickest part approaches a roughly paraboloidal or conical shape.

For disc thicknesses, corrections for advection were calculated using expression (23) for radial shift. In reality the radial advection correction to the pressure inside the disc should be smaller because the thermal energy released inside the disc has an immediate effect upon the local pressure but delayed effect upon the flux coming out from the disc surface. Future calculations of vertical disc structure should take this into account together with radial diffusion of radiation and other effects connected to the two-dimensional nature of thick accretion discs. The general effect upon the vertical scale is smearing the abrupt decrease in disc thickness near the inner radius. The shape of the disc surface generally becomes closer to $h/r =$ const.

3.7 Efficiency

Increasing mass accretion rate limit does not necessarily mean larger luminosity because some part of the energy dissipated inside the disc is advected inwards. Since $\dot{m} \gg 1$, the energy is trapped in the accreting flow even inside the last stable orbit. Indeed, the vertical optical depth in the nearly free-fall region inside the last stable orbit is

$$\tau_z = \varkappa \int_0^z (-u_i k^i) \rho \mathrm{d}\lambda, \tag{29}$$

where λ is affine parameter increasing along the photon trajectory and $k^i = \mathrm{d}x^i/\mathrm{d}\lambda$. Mass conservation implies $\Sigma = \dot{M}/4\pi R u^r$. For a vertical trajectory, $\mathrm{d}r = 0$ and $\mathrm{d}\theta = 0$, and hence, if $u^z = 0$

$$\tau_z = \varkappa \Sigma E = \frac{E\dot{m}}{2ru^r}, \tag{30}$$

where $E = -u_t$ is energy at infinity for a unit-mass particle in the flow. The locally measured diffusion time is $t_{\rm diff} \sim H\tau_z/c$. Radiation diffuses in vertical direction, but in radial direction it is advected at the local dynamical time-scale $t_{\rm dyn} \simeq c(r_{\rm ISCO} - r_{\rm hor})$, where $r_{\rm ISCO}$ and $r_{\rm hor}$ are the radii of the last stable orbit and the event horizon of the black hole, and the infall velocity was set to c. Relative importance of the two effects is given by the time ratio

$$\frac{t_{\rm diff}}{t_{\rm dyn}} \simeq \frac{E\dot{m}}{2(r_{\rm ISCO} - r_{\rm hor})} \frac{H}{R} \sim \dot{m}. \tag{31}$$

This means that the falling flow inside the last stable orbit starting from moderate accretion rates $\dot{m} \sim 1$ is indeed optically thick to electron scattering, especially for higher rotation parameters when the radial free-fall time is small. Optical depths to different absorption processes are likely smaller than unity but are sensitive to clumping (all the opacities that scale with density squared) or to magnetic field strength (synchrotron absorption) and hence are more difficult to constrain. Below in Section 3.8 we estimate the effective optical depth to free–free absorption.

Since the flow is optically thick one can apply the formalism we used in Section 3.4. The energy released in the disc will be shifted downstream by

$$\Delta r \simeq u^r t_{\rm diff} \simeq \frac{1}{2}\mu_0 \dot{m} E. \tag{32}$$

This allows not only to estimate the overall efficiency but also the corrections to the spectral energy distribution that we will present in Section 3.8.

Accretion disc luminosity is given as

$$L_{\rm max} \simeq L_{\rm Edd}\eta(a, \dot{m}_{\rm cr})\dot{m}_{\rm cr}(a) \simeq \\ \simeq 1.4 \times 10^{38} \left(\frac{M}{\mathrm{M}_\odot}\right) \eta(a, \dot{m}_{\rm cr})\dot{m}_{\rm cr}(a) \mathrm{erg\,s^{-1}}. \tag{33}$$

For a thin disc (see, for instance, Shapiro & Teukolsky 1986, section 12.7)

$$\eta(a, \dot{m} = 0) = 1 - \sqrt{1 - \frac{2}{3r_{\rm in}}}. \tag{34}$$

In the general case, $\eta = 1 - E$, where energy E is calculated at the inner visible edge of the disc. Considered in the delayed radius formalism, E should be taken at a radius larger than the last stable orbit radius. For our model thick disc with advection, the large optical depth of the falling flow implies

$$\eta(a, \dot{m}) = 1 - E(r_{\rm hor} + \delta r). \tag{35}$$

Assuming Keplerian rotation allows to approximate the energy as (cf. Page & Thorne 1974, our estimate here does not account for radial motions that should be slow as long as Keplerian rotation holds)

$$E = \frac{\mathcal{G}}{\sqrt{\mathcal{C}}}, \tag{36}$$

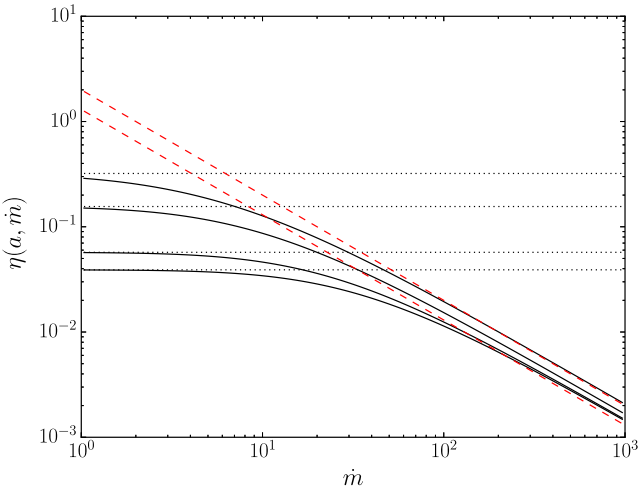

Figure 9. Efficiency dependence on mass accretion rate calculated in delayed radius approximation for different Kerr parameters ($a = -0.9$, 0, 0.9 and 0.998, shown by black solid lines, from bottom to top). Dotted lines are thin-disc efficiencies for corresponding Kerr parameters. Red dashed straight lines are $1.3/\dot{m}$ and $2/\dot{m}$.

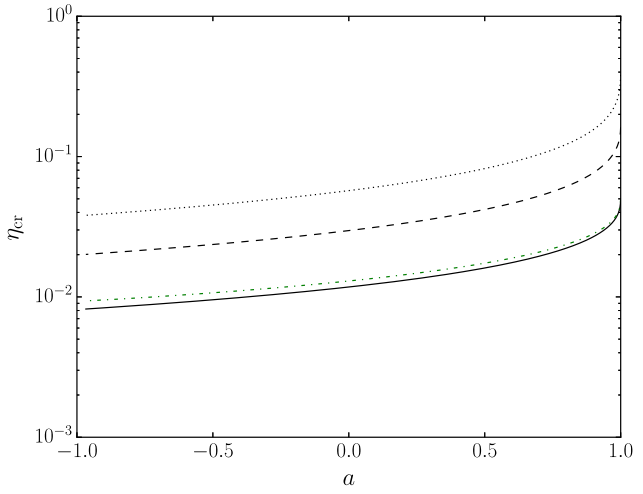

Figure 10. Efficiencies for a thin disc (dotted), thin disc with advection (dashed) and thick disc with advection (solid black and dot–dashed green lines). The green curve also takes into account the radiation escaping from inside the last stable orbit. The three latter curves were calculated for corresponding critical mass accretion rates.

where

$$\mathcal{G} = 1 - \frac{2}{r} + \frac{a}{r^{3/2}}. \tag{37}$$

Efficiency starts decreasing significantly from $\dot{m} \sim 10$ and then approaches a power-law asymptotic $C/\dot{m}$ with C depending upon Kerr parameter. For high mass accretion rates, this implies a constant luminosity of $CL_{\rm Edd}$ with C between approximately 1.3 and 2 (see Fig. 9). When mass accretion rate reaches the critical value and the upper layers of the disc become unbound, efficiency becomes smaller than for the standard thin disc by a factor of about 5 (see Fig. 10). Some, not very large, part of this luminosity is emitted from the disc extension inside the last stable orbit. As advection enters non-linear regime, and the disc starts losing its matter, a logarithmical correction to this quantity should appear that we will discuss in more detail in Section 4.

3.8 Spectral energy distribution

As one can see from previous sections, including thickness effects makes the flux generally higher for intermediate mass accretion rates and lower for $\dot{m} \gtrsim 100$. Thus, the spectral energy distribution first becomes hotter, then cooler with mass accretion rate. We have considered spectral energy distribution of a multi-blackbody disc for a fixed configuration (Schwarzschild black hole viewed at 30° inclination). Public code GEOKERR (see Dexter & Agol 2009 for description) was used to compute the geodesics, and the observed intensity was recalculated using the conservation of energy and angular momentum along the trajectories. Details of intensity transformation may be found, e.g. in section 3.3 of Abolmasov & Shakura (2012b). Black hole mass was set to $M = 10\,{\rm M}_\odot$. For different mass accretion rates, spectral energy distributions were calculated with and without considering thickness effects. For every spectrum, we calculated integral luminosity and position of the maximum of νF_ν (flux per logarithmic frequency interval). The resulting luminosity–temperature plot is given in Fig. 11.

Because in our model the disc retains its multi-blackbody nature, it does not shift significantly from the standard disc luminosity–temperature relation. Most of the luminosity is emitted within the area comparable to the area subtended by the last stable orbit hence the luminosity is always proportional to the local flux in the inner parts of the disc and $L \propto T_{\rm max}^4 \sim E_{\rm max}^4$, where $E_{\rm max}$ is the energy where the spectral energy distribution has the maximum. In Fig. 11, solid curve is the approximate temperature in the disc without correction factors:

$$T_{\rm max} = 5.29 \left(\frac{\dot{m}}{M_1}\right)^{1/4} r_{\rm in}^{-3/4}\,{\rm keV}. \tag{38}$$

For the set of parameters we use here, $T_{\rm max} \simeq 2\dot{m}^{1/4}$ keV.

Strong differences (more than 10 per cent for luminosity, 5 per cent for the maximal energy) in the spectral energy distributions appear above $\dot{m} \simeq 25$ and rapidly increase with the mass accretion rate. This is considerably lower than the $\dot{m}_{\rm cr} \sim 100$ Eddington limit.

Here we assume that all the energy is released in the disc and that all the radiation is thermalized. First assumption is not strictly true because viscous stresses should be present everywhere throughout the transonic flow (see simulations by Shafee et al. 2008; Penna, Sądowski & McKinney 2012). The energy released in the inner parts of the flow contributes to the temperature of the gas and ultimately to Comptonization of the soft radiation of the disc. We do not expect the optical depth of the flow to true absorption to be significantly large. Following Rybicki & Lightman (1986), one can write down the free–free absorption cross-section for fully ionized hydrogen plasma as

$$\sigma_{\rm ff} \simeq \frac{4{\rm e}^6}{3m_{\rm e}c}\sqrt{\frac{2\pi}{3mkT}}n_{\rm e}\frac{1-{\rm e}^{-h\nu/kT}}{\nu^3}, \tag{39}$$

where $n_{\rm e}$ is electron density that may be substituted as

$$n_{\rm e} \simeq \frac{\dot{M}}{4\pi H R u^r m_{\rm p}} \simeq \frac{c^2}{GM\sigma_T}\frac{R}{H}\frac{\dot{m}}{u^r} \tag{40}$$

that implies the effective optical depth of

$$\tau_{\rm eff} \simeq \tau_z\sqrt{\frac{\sigma_{\rm ff}}{\sigma_{\rm T}}} \simeq$$
$$\simeq 5\times10^{-3}\frac{\dot{m}^{3/2}E}{r^2(u^r)^{3/2}}\left(\frac{H}{R}\right)^{-1/2}\left(\frac{T}{\rm keV}\right)^{-1/4}\left(\frac{E}{\rm keV}\right)^{-3/2}. \tag{41}$$

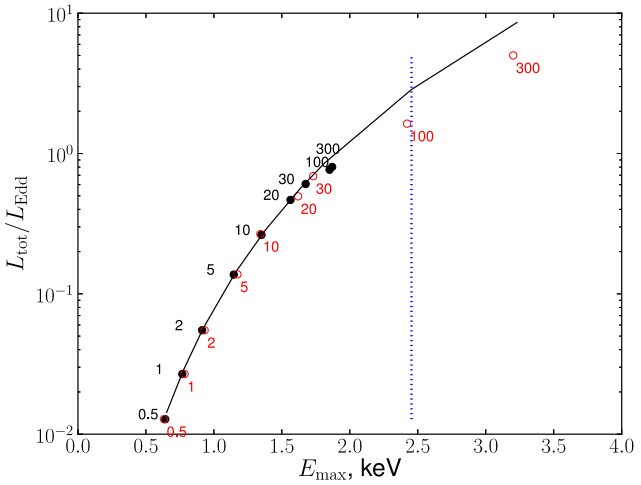

Figure 11. Temperature–luminosity plot (energy of maximal νL_ν in the spectrum was used as a measure of temperature) for black hole accretion discs with different mass accretion rates between 0.1 and 500 spaced evenly in logarithmic space. Dimensionless mass accretion rates are given as black and red numbers. Black circles are for a thick advection-modified disc, red open circles for a thin standard disc. Solid curve corresponds to the approximate relation for a standard accretion disc, where $L \propto E_{\rm max}^4$. Dotted curve is an estimate for the maximal effective temperature expected in discs with outflows.

For a broad range of parameter values ($E \sim T \sim T_{\rm max}$) including the critical mass accretion rates estimated in this work, the effective optical depth is $\tau_{\rm eff} \ll 1$.

4 DISCUSSION AND CONCLUSIONS

4.1 Limits of the standard disc approximation

We considered the balance of forces acting upon a test particle on the surface of a thick disc. Apart from radiation pressure due to electron scattering there are other forces that can induce launching winds from an accretion disc including magnetic stresses and radiation pressure in emission lines (see Proga 2007 for review about line-driven disc winds in AGNs) hence it is probable that in fact any disc is forming outflows even below the Eddington limit. However, the continuum (at least, electron scattering) optical depth of the outflow may become considerably high only above the critical accretion rate limit (relevant optical depth estimates are given by Poutanen et al. 2007, equations 29 and 31).

One of the main questions in the studies of supercritical accretion is the relative importance of energy advection and matter loss. The two limiting cases are the outflow-regulated accretion model introduced by Shakura & Sunyaev (1973) and the totally conservative slim disc model (see Sądowski 2011 for review) in which the larger part of thermal energy released by viscous stresses is advected inwards and finally lost in the black hole. Both models predict lower accretion efficiency (per unit mass in-flowing at large distance) and luminosity exceeding the Eddington limit by a logarithmic factor. Similar logarithmic factor $\ln\left(\frac{R_{\rm out}}{R_{\rm in}}\right)$ arises if one integrates the locally Eddington flux $\propto r^{-2}$ upon the surface of a disc with the outer and inner radii equal to $R_{\rm out}$ and $R_{\rm in}$. Another effect usually neglected in accretion disc calculations but probably important for thick discs is radial radiation diffusion. This process tends to redistribute the radiation flux according to von Zeipel rule (von Zeipel 1924) $F \propto g$ (flux proportional to local gravity) that scales identically with the local Eddington limit. Hence there are different reasons for supercritical discs to attain the $T_{\rm eff} \propto r^{-1/2}$ asymptotic for the supercritical regime and the following logarithmic luminosity growth and 'flat' spectrum ($\nu L_\nu \simeq$ const), and individual effects are difficult to disentangle.

We find that transition to supercritical regime already appears for considerably large advection: only about 10 per cent of the energy released in the disc can escape as radiation and involved in acceleration of disc winds. This justifies the use of models like Lipunova (1999) and Poutanen et al. (2007) that include both outflows and advection. In such models, the mass accretion rate upon the black hole is considerably lower but still of the same order with the inflow rate at the outer rim of the disc. The overall radiative efficiency of mass accretion is probably close to 0.01–0.02 with respect to the mass absorbed by the black hole.

4.2 Comparison to the slim disc model

Our consideration still does not account for some other effects that become important close to the limit. First, the transonic nature of the thick disc solution that is incorporated in the slim disc solution was not considered here. On the other hand, the slim-disc model does not account for the vertical structure but rather operates with vertically averaged equations. In Sądowski et al. (2011), the vertical structure of a slim disc was considered. However, the vertical structure itself was in this paper assumed to be decoupled from the radial structure of the disc, the vertical epicyclic frequency (corresponding to Ω_z or Ω_μ of the present work) was assumed to be constant with the vertical coordinate z, as well as all the velocity components, that means that the disc was in fact treated as thin. This allows to view our model as complementary to the slim disc.

Another difference with the slim-disc approach is our unconventional treatment of advection effects. If advection is the primary term that breaks the local equilibrium between dissipated and radiated energy, and the advection effect is small, it is natural to describe advection as a delay term in the energy conservation equation:

$$Q^+ - Q^- = (\mathbf{v}\nabla)U, \tag{42}$$

where U is the local surface energy density, and Q^+ and Q^- are the flux generated inside the disc and lost by its surface. One can approximate $Q^- \simeq U/t_{\rm diff}$ and arrive to the approximate relation

$$Q^+ \simeq \left(1 + \frac{v_r}{t_{\rm diff}}\frac{\partial}{\partial r}\right) Q^-, \tag{43}$$

or, in a linear approximation,

$$Q^+(r + \delta r) \simeq Q^-(r), \tag{44}$$

where δr is the radial correction introduced in Section 3.4. Besides, this approach has the clear physical meaning that the photons generated at some radius drift downstream before being radiated. Of course, this is a linear approach. For strong advection, the classical treatment of advection as storage of some fixed part of the locally generated heat may prove to be more relevant. In this sense, we also find our model complementary to the slim-disc model.

4.3 Observational implications

It is often adopted for simplicity that the properties of accretion discs change abruptly above the critical mass accretion rate. However, it

seems that for a large span of dimensionless mass accretion rates, approximately between 1 and 100, accretion may be considered close to standard but already altered by thickness and advection. Besides, for $\dot{m} \gtrsim 1$, the optically thick part of the disc extends further inwards that is extremely important in continuum fitting. Detailed continuum fitting is important for estimating black hole spins (Li et al. 2005; Narayan & McClintock 2012). Black hole spins are measured in the high, or soft, states associated with higher mass accretion rates with $\dot{m} \sim 1$ (Meyer, Liu & Meyer-Hofmeister 2000a). For $\dot{m} = 1$, corrections for vertical gravity and advection are unimportant, but rapidly increase with $\dot{m}$. In future, more comprehensive models they should be taken into account together with the effects of radiation transfer and scattering in the inner parts of the flow. Since the inner disc edge is effectively shifted closer to the event horizon one should expect ignoring the radial advection to overestimate the spin of the black hole.

Bright quasars and quasi-stellar objects (QSOs) could be another group of objects that exist close to the criticality limit. The puzzling 5 per cent accretion efficiency required by some observational data such as quasar microlensing (Morgan et al. 2010) may be connected to mild advection effects lowering the radiative efficiency of QSO accretion discs.

4.4 Conclusions

We summarize that, due to stronger vertical gravity, transition to super-Eddington accretion should appear at higher mass accretion rates. Close to the local Eddington limit, disc thickness becomes large and several effects neglected in the standard disc model become important. Here, we estimate the effects of vertical gravity dependence on vertical coordinate and the effects of non-local emission of the energy released in the disc. The latter is primarily connected to radial advection. We find that including both effects simultaneously tends to further increase the local Eddington limit, but the efficiency of accretion decreases to about 1–2 per cent for the critical mass accretion rate. More comprehensive studies taking into account the non-one-dimensional character of thick accretion disc structure are needed to decide upon the relative importance of different effects such as advection and outflow formation in accretion discs exceeding the Eddington limit. It may turn in fact that there is no unique Eddington limit, but accretion disc properties change much more gradually with mass accretion rate.

ACKNOWLEDGEMENTS

We wish to thank Juri Poutanen and Nikolai Shakura for valuable discussions. PA thanks Dynasty Foundation and Academy of Finland grant 268740 for support, AC thanks Finnish Centre for MObility Exchange (CIMO). We are grateful to the anonymous referee for comments and suggestions that helped improve our paper. We also acknowledge support from Russian Foundation for Basic Research grant 14-02-91172.

REFERENCES

Abolmasov P., 2014, MNRAS, 445, 1269
Abolmasov P., Shakura N. I., 2012a, MNRAS, 427, 1867
Abolmasov P., Shakura N. I., 2012b, MNRAS, 423, 676
Abramowicz M. A., 1971, Acta Astronom., 21, 81
Abramowicz M. A., Czerny B., Lasota J. P., Szuszkiewicz E., 1988, ApJ, 332, 646
Abramowicz M. A., Lanza A., Percival M. J., 1997, ApJ, 479, 179
Chakrabarti S. K., 1990, MNRAS, 245, 747
Dexter J., Agol E., 2009, ApJ, 696, 1616
Done C., Gierliński M., Kubota A., 2007, A&AR, 15, 1
Eddington A. S., 1925, MNRAS, 85, 408
Fishbone L. G., Moncrief V., 1976, ApJ, 207, 962
Friedman J., Stergioulas N., 2013, Rotating Relativistic Stars. Cambridge Monographs on Mathematical Physics. Cambridge University Press, Cambridge
Gammie C. F., McKinney J. C., Tóth G., 2003, ApJ, 589, 444
Lawrence A., 2012, MNRAS, 423, 451
Li L.-X., Zimmerman E. R., Narayan R., McClintock J. E., 2005, ApJSS, 157, 335
Lipunova G. V., 1999, Astronom. Lett., 25, 508
Meyer F., Liu B. F., Meyer-Hofmeister E., 2000a, A&A, 354, L67
Meyer F., Liu B. F., Meyer-Hofmeister E., 2000b, A&A, 361, 175
Morgan C. W., Kochanek C. S., Morgan N. D., Falco E. E., 2010, ApJ, 712, 1129
Narayan R., McClintock J. E., 2012, MNRAS, 419, L69
Narayan R., Yi I., 1995, ApJ, 444, 231
Noble S. C., Gammie C. F., McKinney J. C., Del Zanna L., 2006, ApJ, 641, 626
Novikov I. D., Thorne K. S., 1973, in Dewitt C., Dewitt B. S., eds, Black Holes (Les Astres Occlus) Astrophysics of Black Holes. Gordon & Breach, New York, p. 343
Page D. N., Thorne K. S., 1974, ApJ, 191, 499
Penna R. F., McKinney J. C., Narayan R., Tchekhovskoy A., Shafee R., McClintock J. E., 2010, MNRAS, 408, 752
Penna R. F., Sądowski A., McKinney J. C., 2012, MNRAS, 420, 684
Penna R. F., Kulkarni A., Narayan R., 2013, A&A, 559, A116
Poutanen J., Lipunova G., Fabrika S., Butkevich A. G., Abolmasov P., 2007, MNRAS, 377, 1187
Proga D., 2007, in Ho L. C., Wang J.-W., eds, Astronomical Society of the Pacific Conference Series Vol. 373, The Central Engine of Active Galactic Nuclei. Astron. Soc. Pac., San Francisco, p. 267
Riffert H., Herold H., 1995, ApJ, 450, 508
Rybicki G. B., Lightman A. P., 1986, Radiative Processes in Astrophysics. Wiley, New York
Shafee R., McKinney J. C., Narayan R., Tchekhovskoy A., Gammie C. F., McClintock J. E., 2008, ApJ, 687, L25
Shakura N. I., Sunyaev R. A., 1973, A&A, 24, 337
Shapiro S. L., Teukolsky S. A., 1986, Black Holes, White Dwarfs and Neutron Stars: The Physics of Compact Objects. Wiley, New York
Sądowski A., 2011, preprint (arXiv:1108.0396)
Sądowski A., Abramowicz M., Bursa M., Kluźniak W., Lasota J.-P., Różańska A., 2011, A&A, 527, A17
Sądowski A., Narayan R., McKinney J. C., Tchekhovskoy A., 2014, MNRAS, 439, 503
Tassoul J., 2000, Stellar Rotation. Cambridge Astrophysics. Cambridge Univ. Press, Cambridge
von Zeipel H., 1924, MNRAS, 84, 665

APPENDIX A: KEPLERIAN VON ZEIPEL CYLINDERS IN KERR METRIC

A1 Basic equations

Let us assume that dimensionless angular momentum $l = -u_\varphi/u_t$ and angular velocity $\omega = u^\varphi/u^t$ depend on each other unambiguously, $l = l(\omega)$. Note that l here is the angular momentum *per unit energy* rather than per unit rest mass. This is the case for barotropic flows where gradients of pressure and density are collinear everywhere. This sentence is known as Poincaré–Wavre theorem and is proven both for classical mechanics (see Tassoul 2000) and for GR (Friedman & Stergioulas 2013). Sometimes it is also referred to as von Zeipel theorem (Abramowicz 1971; Chakrabarti 1990).

Surfaces of constant l and ω coincide (Chakrabarti 1990) and are known as von Zeipel cylinders. Their shapes however rely upon the given relation between l and ω.

Let us assume that the accretion disc is strictly Keplerian in the equatorial plane:

$$\omega = \omega_{\rm K} := \frac{1}{r^{3/2} + a}, \tag{A1}$$

$$l = l_{\rm K} := \frac{r^2 - 2a\sqrt{r} + a^2}{r^{3/2} - 2\sqrt{r} + a}. \tag{A2}$$

Expression (A1) allows to exclude the radius $r = (\omega^{-1} - a)^{2/3}$ and evaluate angular momentum as a function of ω:

$$l(\omega) = \frac{(1 - a\omega)^{1/3}(1 - 3a\omega) + a^2\omega^{4/3}}{\omega^{1/3}\left(1 - 2(1 - a\omega)^{1/3}\omega^{2/3}\right)}. \tag{A3}$$

Angular velocity may be then found as a function of the two spatial coordinates by solving the equation:

$$l(\omega) = -\frac{g_{\varphi t} + \omega g_{\varphi\varphi}}{g_{tt} + \omega g_{\varphi t}}, \tag{A4}$$

where the left-hand side applies equation (A3), while the right-hand side is a consequence of velocity conversion relations $u_\varphi = g_{\varphi t}u^t + g_{\varphi\varphi}u^\varphi$, $u_t = g_{tt}u^t + g_{\varphi t}u^\varphi$. Relevant metric coefficients

$$g_{tt} = -1 + \frac{2r}{\rho^2}, \tag{A5}$$

$$g_{\varphi t} = -\frac{2ar(1 - \mu^2)}{\rho^2}, \tag{A6}$$

$$g_{\varphi\varphi} = \frac{\Sigma^2}{\rho^2}\left(1 - \mu^2\right), \tag{A7}$$

where

$$\mu^2 = \cos^2\theta, \tag{A8}$$

$$\rho^2 = r^2 + a^2\mu^2, \tag{A9}$$

$$\Sigma^2 = (r^2 + a^2)^2 - a^2\Delta\left(1 - \mu^2\right), \tag{A10}$$

$$\Delta = r^2 + a^2 - 2r. \tag{A11}$$

Finally, the main equation for angular velocity becomes

$$\frac{(1 - a\omega)^{1/3}(1 - 3a\omega) + a^2\omega^{4/3}}{\omega^{1/3}\left(1 - 2(1 - a\omega)^{1/3}\omega^{2/3}\right)} = \frac{\Sigma^2\omega - 2ar}{\frac{\rho^2 - 2r}{1 - \mu^2} + 2ar\omega}. \tag{A12}$$

A2 Schwarzschild case

If one sets $a = 0$, it is possible to obtain an analytical expression for angular velocity as a function of r and μ. Equation (A12) becomes

$$\omega^{4/3}\left(1 - 2\omega^{2/3}\right) = \frac{r - 2}{(1 - \mu^2)r^3}. \tag{A13}$$

This equation is cubic both in r (useful for recovering the shapes of the cylinders) and in $f = \omega^{2/3}$

$$f^3 - \frac{1}{2}f^2 + X = 0, \tag{A14}$$

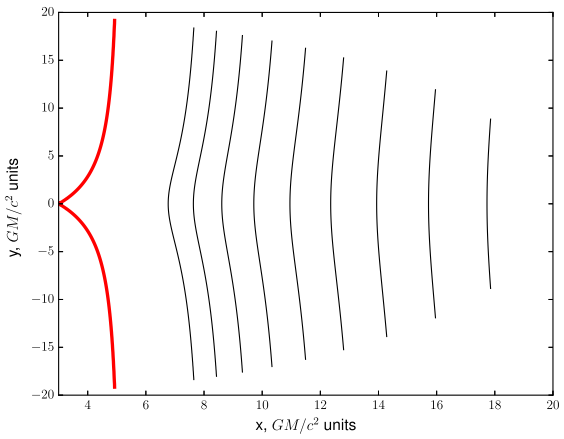

Figure A1. Keplerian von Zeipel cylinders for a Schwarzschild black hole. Red thick line is the applicability limit of the solution given by (A16).

where $X = \frac{r-2}{2(1-\mu^2)r^3}$. This equation is easily transformed into a depressed cubic equation $t^3 + pt + q = 0$ by a substitute $t = f - 1/6$:

$$t^3 - \frac{1}{12}t + \left(X - \frac{1}{108}\right) = 0. \tag{A15}$$

In this equation, $p = -1/12 < 0$. Equation discriminant $D = 4p^3 + 27q^2 < 0$ for any $r > 6$ and $\mu < 1/\sqrt{2}$, hence

$$t = \frac{1}{3}\cos\left(\frac{1}{3}\mathrm{acos}\,(1 - 108X) - \frac{2\pi}{3}\right), \tag{A16}$$

and $\omega = \left(t + \frac{1}{6}\right)^{3/2}$. Keplerian rotation field in the Schwarzschild case is shown in Fig. A1.

A3 General Kerr case: solution and results

Right-hand side of equation (A12) is singular at small ω, but when searching for the solution for given r and μ, one should be conscious about the singularity in the left-hand side of the equation, setting the maximal possible frequency:

$$1 - 2(1 - a\omega_{\rm max})^{1/3}\omega_{\rm max}^{2/3} = 0, \tag{A17}$$

$$\omega_{\rm max}^3 - \frac{1}{a}\omega_{\rm max}^2 + \frac{1}{8a} = 0. \tag{A18}$$

Substituting $\omega_{\rm max} = t + \frac{1}{3a}$, one arrives again to a cubic equation:

$$t^3 - \frac{1}{3a^2}t - \frac{2}{27a^3} + \frac{1}{8a} = 0. \tag{A19}$$

For any $a \neq 0$, $p = -\frac{1}{3a^2} < 0$, $D = \frac{4}{27a^6}(1 + (1 - \frac{27}{16}a^2)^2) > 0$ hence the solution may be expressed as

$$\omega_{\rm max} = -\frac{2}{3a}\mathrm{sign}\left(\frac{1}{8a} - \frac{2}{27a^3}\right) \times \cosh\left(\frac{1}{3}\mathrm{acosh}\left(\frac{3}{16}\left|a\left(1 - \frac{16}{27a^2}\right)\right|\right)\right). \tag{A20}$$

For $0 < \omega < \omega_{\rm max}$, equation (A12) was solved numerically for ω for different r outside the last stable orbit radius and for $|\mu| < \frac{1}{\sqrt{2}}$. Isolines of resulting angular frequency for different Kerr parameter values are shown in Fig. A2.

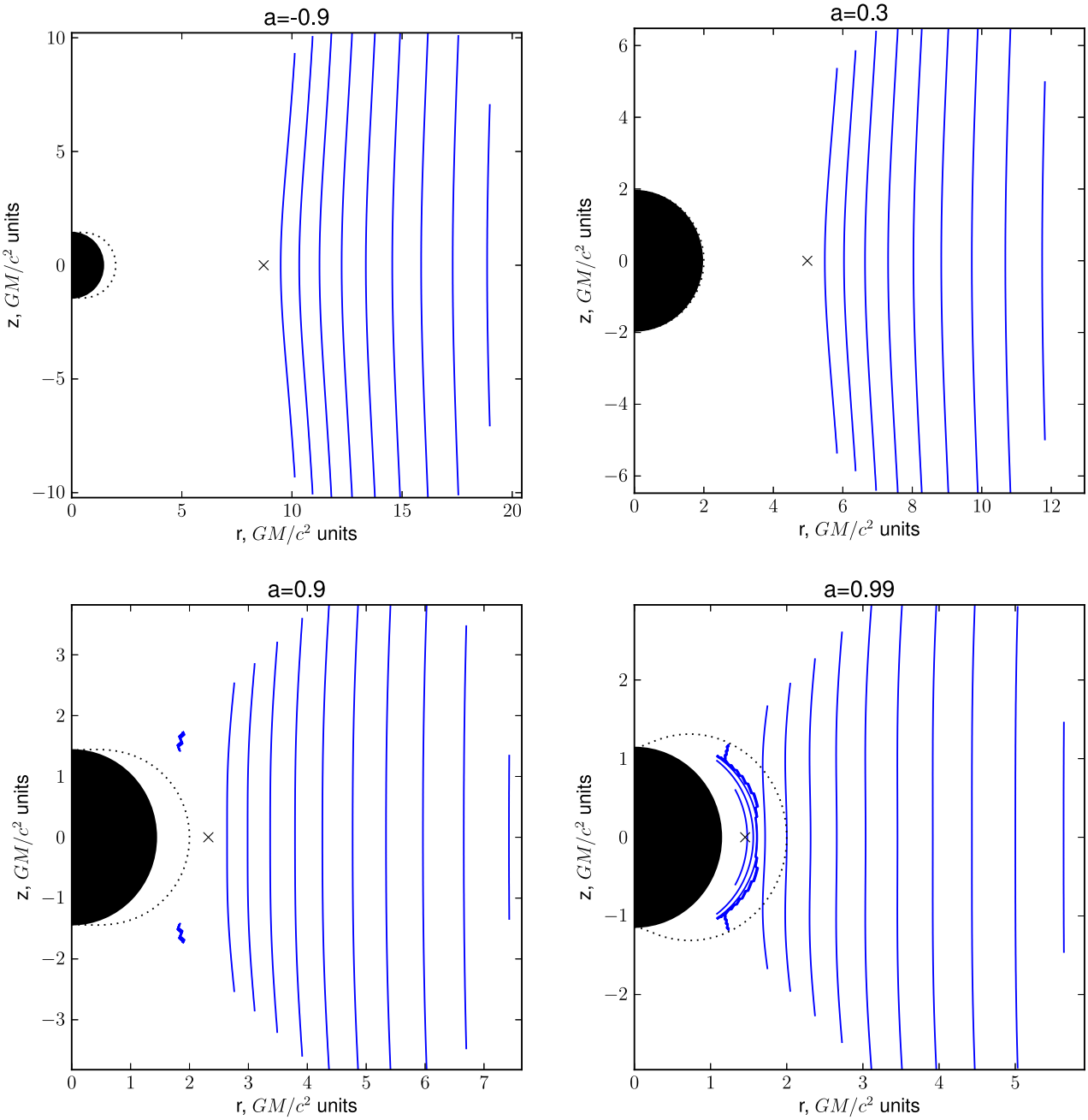

Figure A2. Keplerian von Zeipel cylinders for different Kerr parameters. Dotted curves mark the outer limit of the ergosphere. Cross is the position of the last stable orbit in the equatorial plane.

This paper has been typeset from a TEX/LATEX file prepared by the author.